Chapter 6
Particle-in-cell simulation of an argon plasma

As mentioned in Chapter 1 the energy and angular distribution of the ions at the substrate have a significant effect on the etching process. The form of these distributions will be largely determined by ion-neutral collisions within the sheath, and a considerable number of theoretical and numerical models have been developed in recent years to study this problem. As shown in Chapter 4 collisions between ions and neutrals within the main body of the plasma also have a significant effect on the bulk parameters – there is a substantial increase in the plasma density, a drop in the electron temperature and flattening of the potential profiles, as compared to the case in which ions are collisionless. Pressure is the main determining factor for the degree of collisionality in the plasma, increasing the pressure reduces the ion mean free path, and increases the number of collisions ions make over a given distance. The ratio of ion mean free path/sheath width determines the average number of collisions an ion will make in the sheath, which in turn strongly effect the ion distributions at reactor surfaces.

Recently a number of models have been used to study the effect of collisions on both the energy and angular distribution of ions hitting the electrodes, in particular at the powered electrode, since this is the position of the substrate in RIE etching reactors (Kushner (1985), Thompson *et al* (1988), Liu *et al* (1990), Manenshijn and Goedheer (1991), Wild and Koidl (1991)). Kushner and Wild and Koidl determine the ion energy distribution at the electrode, including only the effects of charge exchange collisions, and using cross sections which are independent of energy. Wild and Koidl find very good agreement between their theoretical IEDs and experimental measurements. Thompson *et al* (1988) determine both energy and angular distributions of SF_5^+ ions in SF_6, using a Monte Carlo model that can include either isotropic (hard sphere) or anisotropic elastic scattering and charge exchange interactions. They find that the distributions do not substantially depend on the elastic cross section, since in the isotropic model ions make a small number of large angle collisions, while in the anisotropic model more small angle collisions are made. Manenschijn and Goedheer (1991) determine impact energy and angular distributions for both ions and neutrals, using isotropically scattered elastic and charge exchange collisions.

According to work in Chapter 5, scattering cross-sections in argon are very anisotropic for high energies, but become much more complex for energies in the range 0.1 to 10 eV. Modelling elastic collisions using hard sphere, isotropic interactions should considerably underestimate small angle scattering effects and overestimate large angle scattering. The results of Thompson *et al* are therefore surprising and need to be investigated further. Particularly since Mason and MacDaniel (1988) suggest that interaction potentials of the form used by Thompson *et al* are not good at predicting the intermediate-range forces which are critical in determining large scattering angles. A further drawback of the Monte Carlo investigations is that they do not self-consistently determine the sheath fields, but instead use an analytic expression, with most assuming linear or averaged electric fields with perfectly sinusoidal variation. This does not properly take into account the periodic variation of the fields, nor the non-linearity introduced by the incursion of the electrons, as discussed in Chapter 3. Using the differential cross-section model in a PIC code allows a fully self-consistent simulation of the ion collision processes taking place in the bulk and the sheath, and hence a better approximation what is really happening in the plasma. This should give a better understanding of the important processes and how these effect the distributions.

Although argon is not typically used as an etchant in RIE applications there are many other theoretical and experimental results available for comparison, as the collision processes are relatively simple, and there are no chemical/dissociation processes to take into account. The availability of detailed cross-section measurements has also allowed development of an accurate model of the ion-neutral collisions (Chapter 5). The PIC simulations were designed in particular to model the system used by Liu *et al* (1990), in which experimental measurements of the ion energy and angular distributions were made at the electrodes of an argon discharge. Liu *et al* (1990) have also derived a Monte Carlo code, which includes differential collision cross-sections for Ar-Ar^+ (determined by fitting to the experimental cross-sections of Vestal *et al.* (1978)), to model the ion distributions. The experimental set-up is described in section 6.1 and results from the PIC simulation are compared in detail to experimental data in Sections 6.2. Some comments are made comparing the relative agreement between the Monte Carlo and PIC models of the ion distributions. In Section 6.3 comparison is made between distributions produced by a simulation using isotropic elastic collisions for the ions, and the simulation results using anisotropic collisions. Section 6.4 concludes the chapter.

6.1 Experimental set-up

A schematic of the experimental apparatus taken from Liu *et al* is shown in Figure 6.1 (a). The system consists of two parallel plate electrodes separated by a 3 cm gap. Each electrode has an area of 0.00117 m^2. A symmetric 1-D PIC code was therefore chosen to model this system - it includes similar features to the spherical model but solves the equations for planar geometry. Experimental results were taken for a peak-peak electrode voltage of 130V, a source frequency of 13.56 MHz and pressures of 10, 50 and 500 mTorr. Similarly simulation results were run with V_{pp} = 130 V, f_{rf} = 13.6 MHz and p = 10, 20, 50, 100 and 500 mTorr.

The ion analyser is shown in Figure 6.1 (b). It is described in detail by Liu *et al.*, so only a brief description is given here, in reference to comments made later in the chapter. The analyser consists of a series of concentric annular rings, which are electrically insulated from one another, and from the current collected by each ring the relative angular distribution can be determined. Each ring has an angular width of about 4.5°, and are positioned at (average) collection angles of 2.3°, 6.8°, 11.3°, 15.8°, 20.3°, 24.8°, 29.3°, 33.8° and 37.3°. Three stainless steel meshes in front of the collection rings can be biased to allow only ions of a specified energy to be detected.

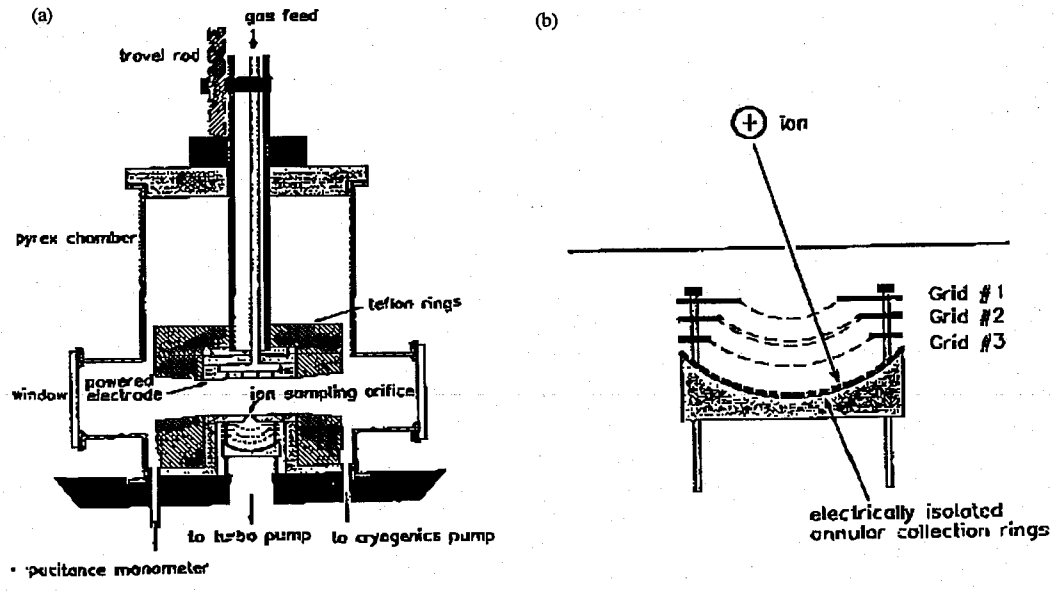

Figure 6.1 Schematic of experimental apparatus used by Liu *et al* (1990) **(a)** shows the reactor system and **(b)** is a detailed view of the detector for the ions. Annular rings are used to determine the angle of incidence and the grids are biased so that only ions of a given energy are recorded.

6.1.1 *Plasma parameters*

Unfortunately the paper does not give many experimental results for the plasma parameters, so it is a little difficult to determine the congruence between simulation and experimental conditions. Liu *et al* do give the sheath width as a function of pressure, and results for both experiment and simulation are plotted in Figure 6.2. Agreement between the two is extremely good, with less than 15 % discrepancy, over the whole pressure range. This is fortunate since good agreement between the sheath widths is necessary to make even a first order comparison between simulated and experimental ion distributions. The simulation results were fitted with a power law, as shown in Figure 6.2, indicating that the sheath width depends on the pressure according to $s \propto p^{-1/4}$.

The average plasma density and the sheath voltage from the simulation are plotted in Figure 6.3. As the pressure increases the mean free path of the charged species in the plasma decreases. This leads to a higher creation rate (from increased ionisation by electrons) and a reduced loss rates (due to a decrease in the ion mobility). Hence the average plasma density increases with pressure. The average sheath potential on the other hand remains constant over the pressure range, since the applied voltage is kept constant.

The dependence of density on pressure has been empirically fitted in Figure 6.3 (a), giving $n_{avg} \propto p^{5/8}$. This, together with the fitting for the sheath width as a function

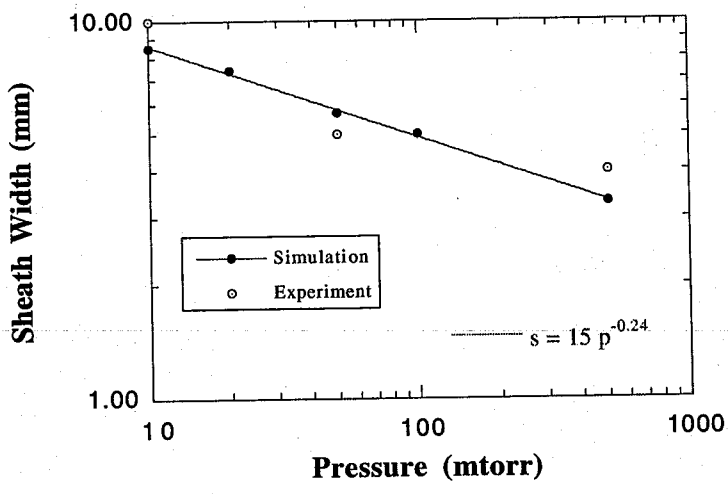

Figure 6.2 Sheath width as a function of background gas pressure showing experimental and simulation results. The simulation results have been fitted with a power law

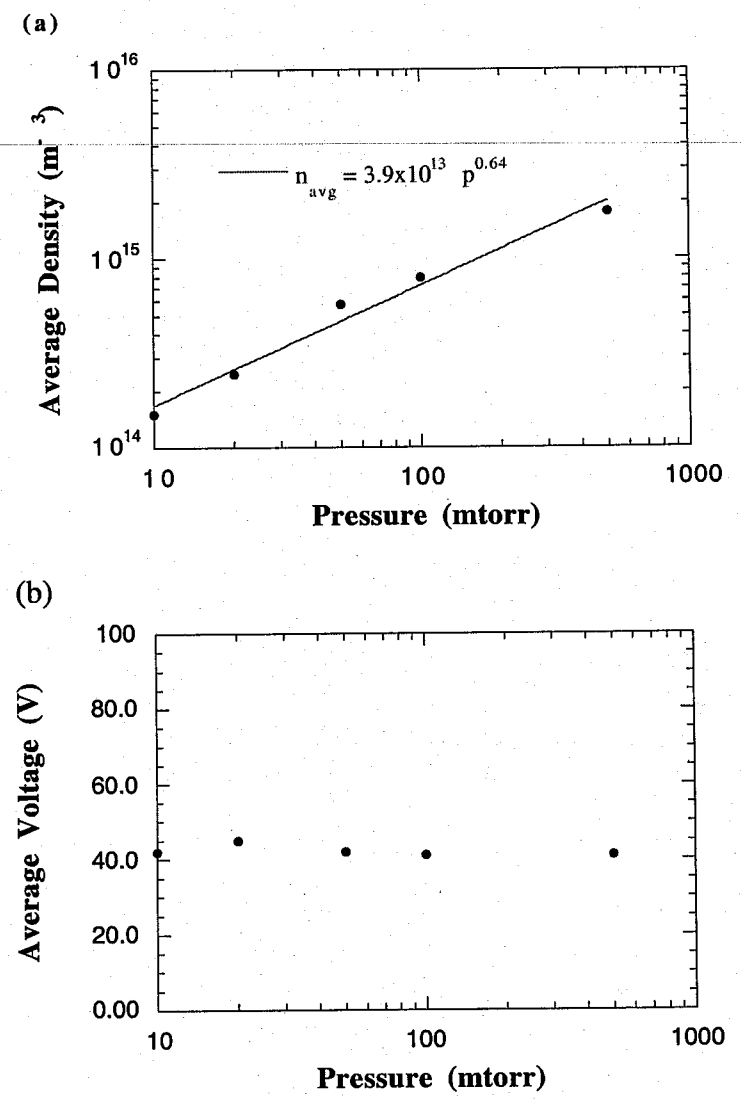

Figure 6.3 Pressure dependence of **(a)** the average plasma density **(b)** the sheath potential.

of pressure, gives the dependance of the sheath width on the average density as $s \propto n^{-2/5}$. Lieberman (1988) calculated the law for a collisional sheath, assuming a constant ion mean free path, and found $n_s u_s \propto V^{3/2} s^{-5/2}$, where n_s and u_s are the ion density and average velocity at the edge of the sheath. Assuming u_s is given by the Bohm criterion and is constant, then, for a constant sheath voltage, this gives the same dependance of the sheath width on density as found from the simulation. Figure 6.3(b) shows that the sheath potential is relatively independent of pressure.

As discussed in Chapter 4 most of the electrons gain most of their energy through interaction with the moving sheath. At low pressures these high energy electrons traverse the plasma, with some making collisions in the centre and others reaching the opposite

sheath. As the pressure increases and the mean free path between the collisions is reduced, the range of the electrons decreases until finally energetic electrons cannot move very far from the sheath before dumping their energy into inelastic collision processes. This effect can be seen very clearly from Figure 6.4 (a), in which the density profiles of electrons with energies greater than the ionisation energy are plotted for different gas pressures. At the lower pressures the average energy is highest in the middle of the plasma, since the mean free path is of the order of the system length and so energetic electrons contributed from each sheath can travel into the centre of the plasma. At 500 mTorr, however, the mean free path is only a few millimetres, and so the electron energy is rapidly reduced by collisions, hence the density peaks close to the sheath edge.

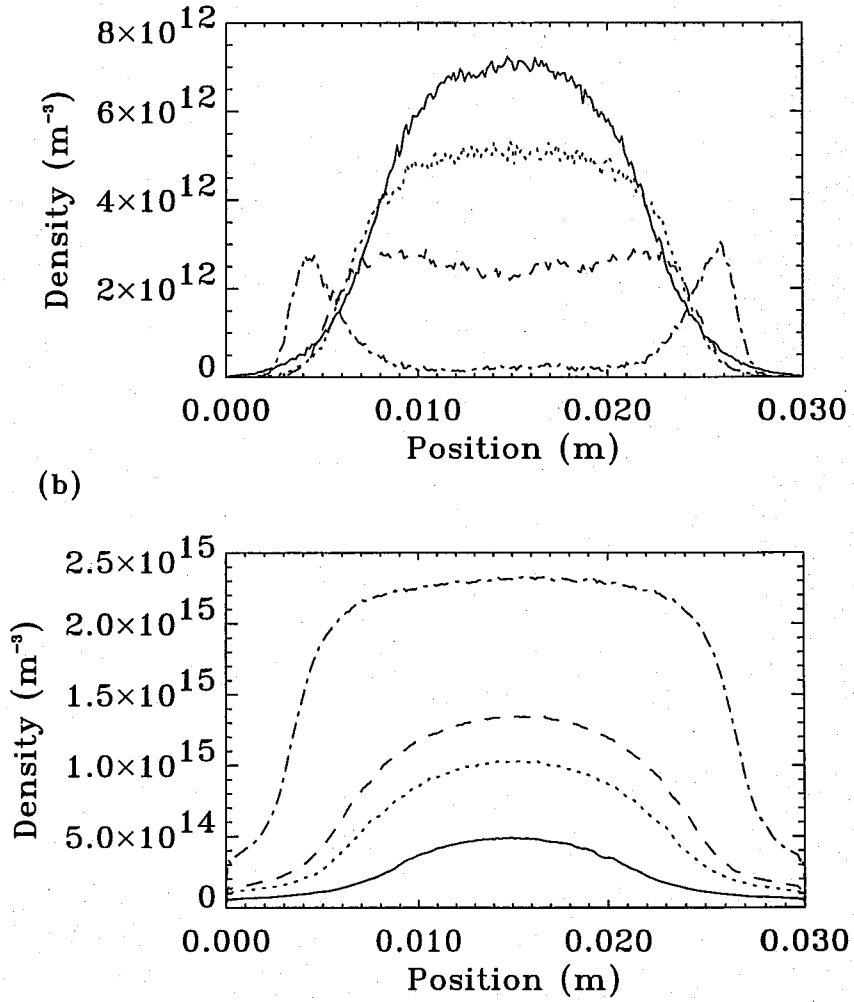

Figure 6.4 Density profiles across plasma for pressures of 20 mTorr (solid line), 50 mTorr (dotted line), 100 mTorr (dashed line), 500 mTorr (dash-dot line) for **(a)** electrons with energies greater than the ionisation energy **(b)** the ion density.

Figure 6.4 (b) shows the corresponding ion density profiles for the different pressures. The form of the ion profile is determined by two factors: where most of the ions are created, and by their mobility. At the low pressures the electron energy peaks in the centre and so this is the region of highest ion creation. High penetration of the pre-sheath fields (as discussed in Chapter 4) and relatively large ion mobilities give the profile quite steeply sloping sides. At high pressures, where most of the ions are created close to the sheath edge, large pre-sheath fields are not required and so the profiles become very much flatter, and there is an increase in density (and a small reduction in the average electron energy)

6.2 Ion Distributions at the Electrode

This section gives a detailed comparison between simulation and experimental results for the ion energy and angular distributions and angle dependent energy distributions at the electrodes. Similarities and differences are discussed in context of the sheath physics and ion interactions within the sheath.

6.2.1 Total energy distributions

Figures 6.5 to 6.7 show the total energy distributions for pressures of 10, 50 and 500 mTorr, for both simulation and experiment. According to Liu *et al* the experimental results are normalised so that the area under each curve is equal, and the simulation results are normalised in a similar fashion so that the area under each curve is 1. In Figure 6.5 (a) it can be seen that at 10 mTorr the experimental results are double peaked. Although this appears similar to IEDFs found in collisionless rf systems, from equation (4.30) the peak separation for these conditions should be about 0.7 eV, so rf peak splitting is an unlikely explanation. It will later be shown that the low energy peak is actually due to ions which have had collisions in the sheath. The high energy peak occurs at an energy of about 36 eV. The simulation result also has a high energy peak close to 40 eV but shows no sign of a low energy peak. The high energy peak is equal to the average voltage across the sheath (see Figure 6.3 (b)) and so represents the average energy for ions crossing the sheath without making collisions. Results from Liu *et al*'s Monte Carlo code (not shown) also display a high energy peak at around 40 eV, but with almost no ions at lower energies. This is probably due to the use of a spatially uniform

electric field in the MC code, resulting in equal acceleration of ions at all positions in the sheath.

Figure 6.6 shows the IEDF for 50 mTorr. The simulation results differ somewhat from the experimental distribution, showing a much steeper decrease in the distribution at higher energies. The peaks in the distribution, which Liu *et al* describe as being very reproducible, are less noticeable – this is partially due to smoothing of the

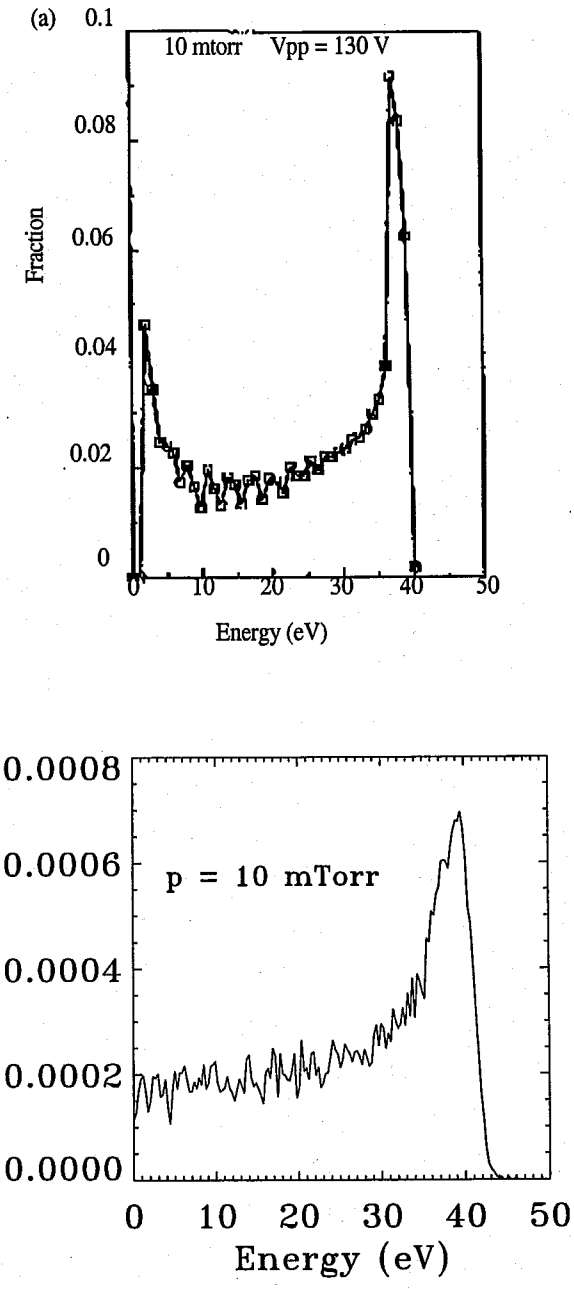

Figure 6.5 Total ion energy distribution at the electrodes, for a pressure of 10 mTorr **(a)** experimental results (Liu *et al* (1990)) and **(b)** simulation. Both curves are normalised as described in the text.

distribution. Computational speed limits the number of ions used to calculate the distribution to around 2000, so the IEDFs tend to be quite noisy and smoothing is used to pick out the main features of the distribution. However the loss of the small high energy peak is not simply due to statistics. This is discussed further, later in the section.

The IEDF at 500 mTorr is plotted in Figure 6.7. The experimental results show a very smooth distribution, peaked at about 6 eV, with a tail of up to 45 eV. Liu *et al* describe this as a fully developed distribution, and state that the shape of the IEDF remains unchanged at higher pressures. Although the simulation results have a similar form – peaked at low energies, tailing down to higher energies – the simulation

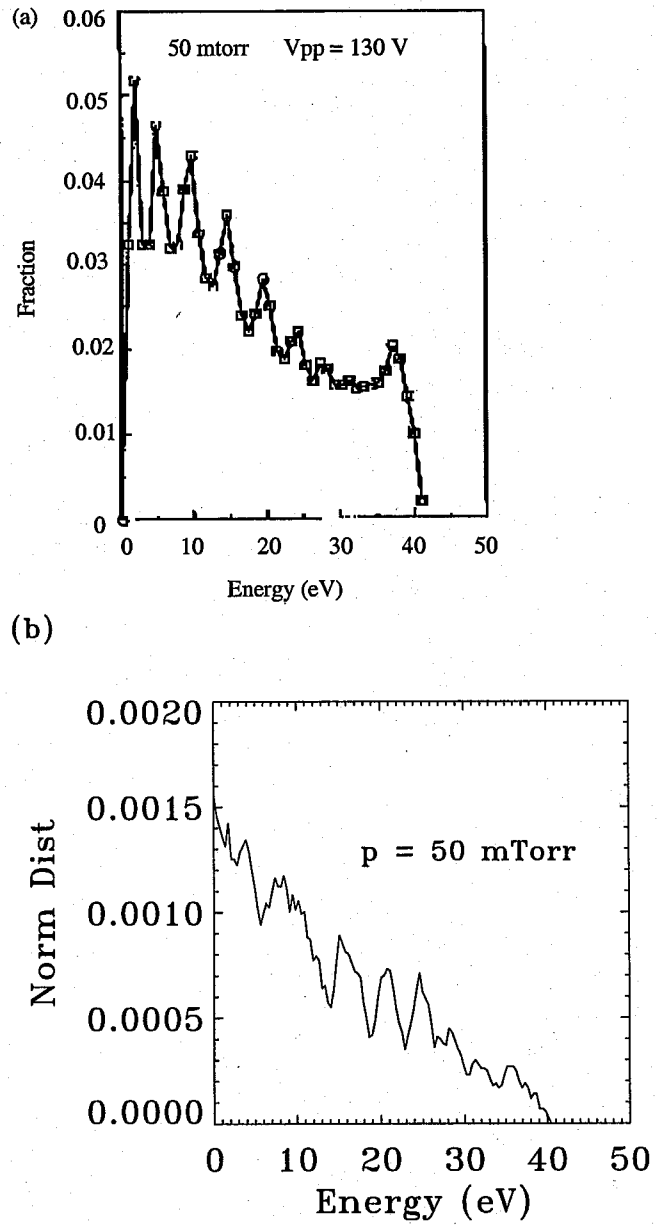

Figure 6.6 Total ion energy distribution (normalised) at the electrodes, at 50 mTorr **(a)** experimental results (Liu *et al* (1990)) and **(b)** simulation

distribution is shifted to *much* lower energies, and has more visible structure. The lowest energy peak occurs at about 1 eV, with a second peak at about 3 eV (and multiple smallerpeaks at higher energies); the maximum energy of ions arriving at the electrode is about 20 eV. At a pressure of 500 mTorr the mean free path between charge exchange collisions is only about 0.2 mm. The electric field in the sheath is approximately 9000 Vm^{-1}, and so ions should gain roughly 2 eV in between collisions. This would explain the small energy peak seen in the simulation IED. The Monte Carlo code similarly shows

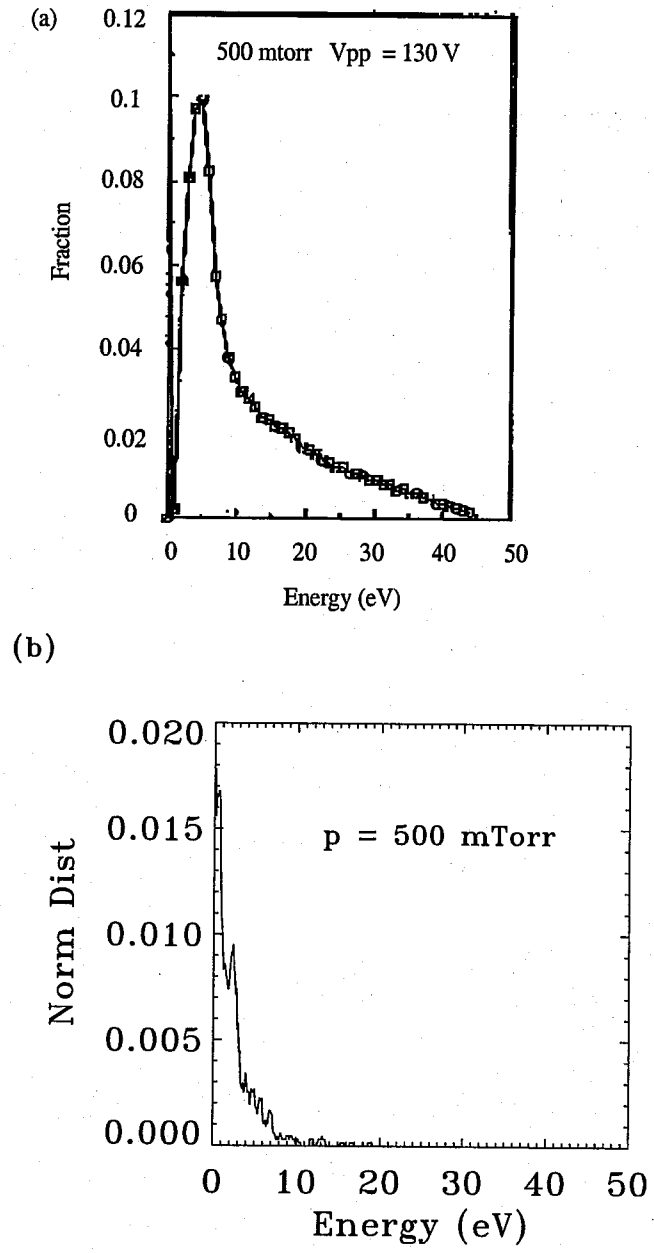

Figure 6.7 Total ion energy distribution (normalised) at the electrodes, at 500 mTorr.**(a)** experimental results (Liu *et al* (1990)) and **(b)** simulation

a shift to much lower ion energies, with peaks at 1 and 2 eV and a maximum energy of 8 eV.

This seems to indicate that the models are producing more collisional IEDs than determined experimentally. As a test of this hypothesis a simulation was run for a pressure of 100 mTorr, to determine the effect on the IED of reducing the number of collisions by a factor of 5. This is plotted in Figure 6.8. At the lower pressure the distribution extends to higher energies and looks much more like the experimental IEDF in Figure 6.7 although with more ions at very small energies ($\leq$ 2 eV), and more structure. The experimental IEDs are unlikely to resolve very low energies, since Liu *et al* report an analyser resolution of 1 - 2 eV, and they say that ions with less than 5 eV are likely to be deflected by electric field distortion at the analyser orifice.

The lack of agreement between the experimental and simulation IEDFs at 500 mTorr (and to a lesser extent 50 mTorr) therefore seems to be due to differences in the number of collisions ions undergo in the sheath. Liu *et al* suggest that the shift to lower energy of the Monte Carlo IED is due to an overestimate in the magnitude of the charge exchange cross-sections at low energies. They use cross-sections which are fitted to the experimental measurements of Vestal *et al* (1978) and must extrapolate the results to low energies. However the differential cross-section model used in the PIC simulations (described in Chapter 5) uses the interaction potential of Ar-Ar^+ to derive the cross-section down to energies of less than 0.001 eV. The accuracy of the cross-section would appear to be confirmed by comparison to drift velocity experiments.

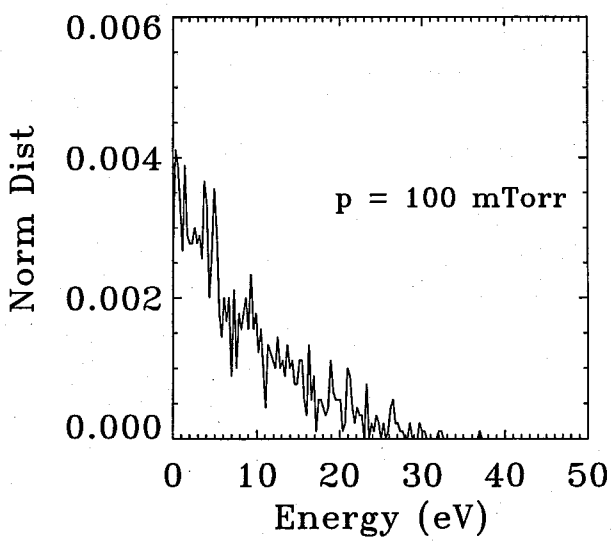

Figure 6.8 Total IEDF at a pressure of 100 mTorr determined from the simulation. than 1 eV the charge exchange probability decreases.

One factor which would affect the distribution is a large difference between the simulated and experimental sheath widths. From Figure 6.2, the experimental sheath measured at 500 mTorr is about 25 % larger than the simulation sheath, which would actually indicate that in the experiment the ions are more likely to make collisions as they travel through the sheath. This would tend to shift the distribution to smaller energies, closer to the simulated distribution.

One curious aspect of the experimental IED is that ions are measured crossing the sheath with the full average potential, which – regarded simplistically – seems very unlikely, since ions should make around 50 collisions while traversing the sheath. It would seem therefore that the simulation is not adequately representing some aspect of the experimental system. Possibly this is due to simplification of the physics used to model the plasma, such as neglecting the presence of doubly ionised argon, or energetic neutrals, in the sheath region and ignoring effects of coloumb collisions. According to Ellis *et al* (1976) Ar^{++} has double the mobility of Ar^{+} in argon, so there is a higher probability of crossing the sheath without making collisions. Ions making charge-exchange collisions with energetic neutrals could possibly gain, rather than lose, energy, particularly if they are at low energies. Another aspect of this is that fast neutrals created by charge exchange will tend to leave the sheath region, and at high pressures this could lead to a reduction in the effective neutral pressure in the sheath (anecdotal evidence of this was given by Dr. R. Porteous, in a hybrid PIC-fluid simulation of an inductive reactor, described in Porteous *et al* (1994), which does include neutrals explicitly).

Conversely, the difference could be related to the experimental apparatus used to measure the IED. There will be some reduction in neutral density just above the ion sampling hole of the ion analyser due to differential pumping, which, if sufficiently large, would artificially increasing the ion mean free path in this region. The sheath fields are quite non-uniform and highest close to the electrode, and so, in theory, ions could gain relatively large energies before entering the analyser. At 100 mTorr the ion mean free path is approximately 2 mm, over which distance the ion can gain approximately 35 eV. This could explain why the experimental results at 500 mTorr are better matched by simulation results at 100 mTorr. Most likely the difference is due to a combination of simplifying both the plasma physics and the reactor system modelled by the simulation.

6.2.2 *Total Angular Distribution*

The total angular distributions at each pressure are plotted in Figure 6.9, with simulation results plotted in direct comparison with the experimental results from Liu *et al.*, which are represented by the stars. Simulation results are normalised so that the area

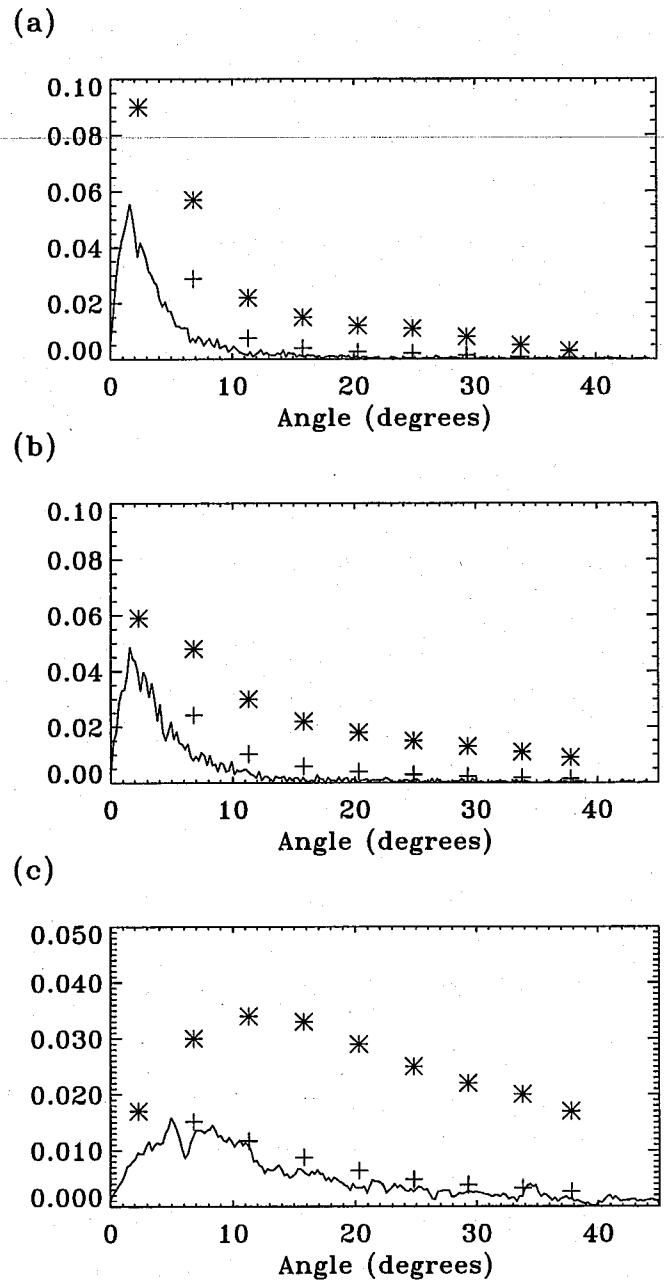

Figure 6.9 Angular distributions showing simulation results (solid line), experimental results (*) and experimental results with area correction (+) for pressures of **(a)** 10 mTorr **(b)** 50 mTorr and **(c)** 500 mTorr

under the curve equals 1. This indicates that simulation results have a similar form but a much smaller magnitude than the experimental measurements, particularly at large angles. A possible reason for the larger measurements in the experimental distribution is the difference in the areas of the annular rings of the analyser – larger angles have larger collection areas and therefore can collect more current. No mention is made in the paper

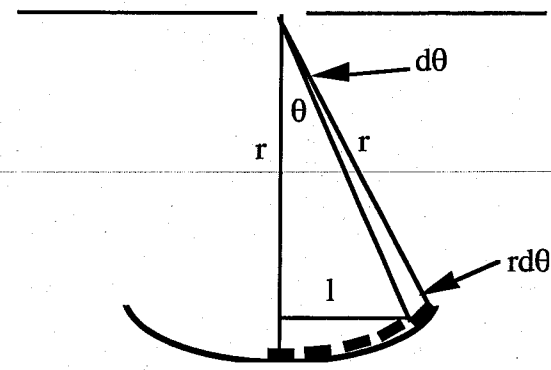

Figure 6.10 Diagramatic representation of the relative area of each annular ring.

of whether or not the relative measurements at the different angles were corrected for this.

Assuming that the ion analyser (shown in Figure 6.10) is approximately spherical then the area of each annular ring is given by

$$A_\theta = 2\pi r\, d\theta\, (r \sin\theta) \qquad (6.1)$$

where θ is the average angle of the collection ring, $d\theta$ is the angular width of the rings and r is the separation between the electrode and the analyser. The area of the central ring is $A_o = \pi(rd\theta)^2$, so the area of a ring at angle θ relative to the central ring is

$$\frac{A_\theta}{A_o} = \frac{2\sin\theta}{d\theta}. \qquad (6.2)$$

The measured angular distribution was divided by (6.2) and re-plotted in Figure 6.9 (as the crosses). Dividing through by the relative area of the rings reduces the IAD, particularly at large angles, resulting in distributions which look much closer to the IADs found from the simulation.

In Figure 6.11 the average energy and average angle of impact are plotted as a function of pressure for both simulation and experiment. The average energy at small pressures is similar for both simulation and experiment, but at higher pressures simulation values are much smaller than those measured experimentally. Hypotheses for this difference have been discussed earlier in this section. Monte Carlo codes by Kushner (1985) and Manenshijn and Goedheer (1991) also find small ion energies at high pressures. Manenshijn and Goedheer predict an average energy of less than 1 eV at 500 mTorr. The average impact angle of the ions is also much smaller for the simulation

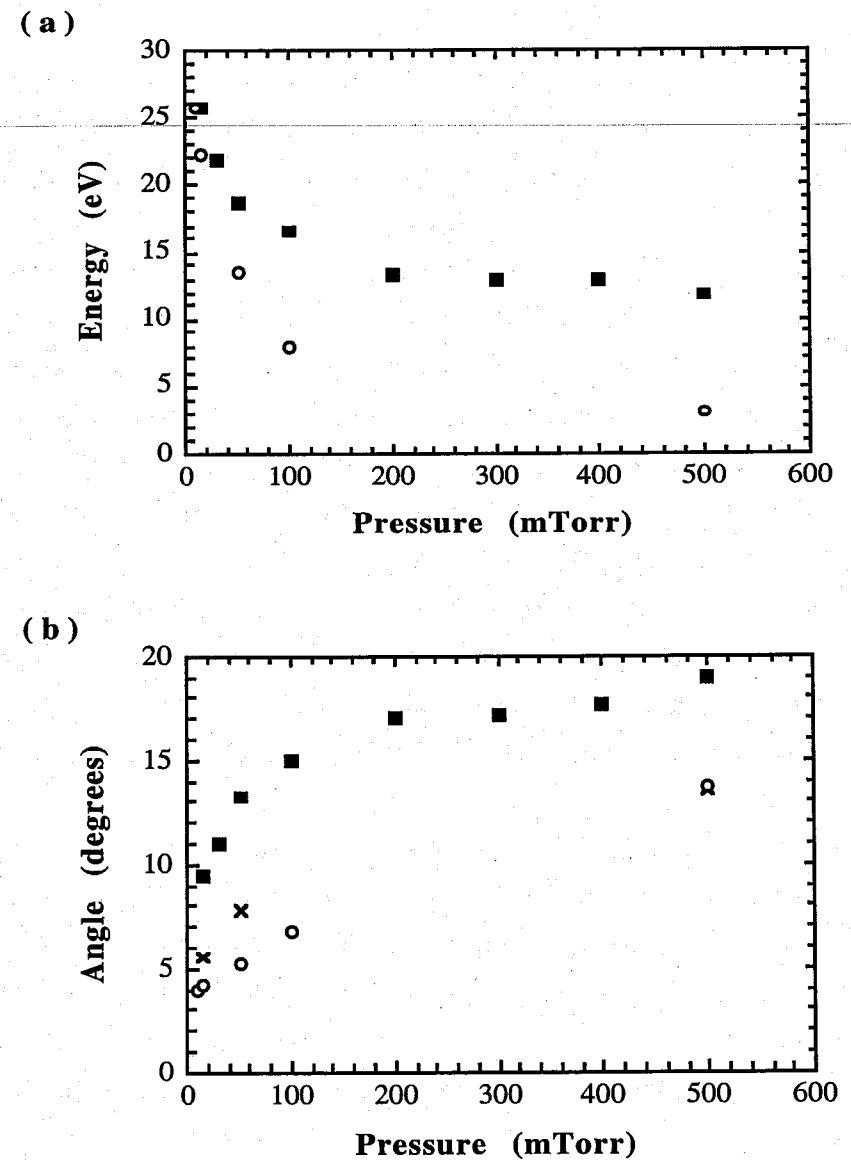

Figure 6.11 Average impact **(a)** energy and **(b)** angle as a function of pressure. Experimental results are shown as filled squares and simulation results as hollow circles. Modified experimental angles (asterix) are obtained by integrating area corrected results from Figure 6.9.

than the experiment, although much better agreement is obtained by integrating the modified experimental results from Figure 6.11 to obtain an average angle (plotted as crosses).

6.2.3 *Angle-dependent energy distributions*

Figures 6.12 - 6.14 below show IEDs measured at specified incident angles, for pressures of 10, 50 and 500 mTorr. In the experimental system the angle subtended by the annular rings is 4.5° and the average angles used for the distributions are 2.3°, 11.3°, 20.3° and 29.3°. In the simulation the ion distributions were similarly binned into angular ranges of 4.5°, with the same average angles.

As seen from Chapter 5 both charge exchange and elastic collisions can change the direction of the ion trajectory. However in a charge exchange collision almost all of the ion energy is transferred to the neutral, producing a thermal ion – in effect charge exchange looks like an elastic collision with a scattering angle close to 180°. A thermal ion created in the sheath will accelerated by the sheath fields, and if it has no further collisions then its parallel energy (i.e., its energy parallel to the field direction) will be much larger than its perpendicular energy at the electrode, so the trajectory will be nearly normal to the electrode surface. The energy it can gain depends on the average potential difference between the electrode and the position at which it was created. Charge exchange collisions (on their own) can therefore shift the IED to lower energies, but have little effect on the IAD.

In elastic encounters a certain amount of energy is transferred from ion to neutral, depending on the scattering angle. Very small scattering angles (< 1°) have little effect on either particle, but in large scattering angle collisions a substantial amount of energy is transferred to the neutral, and the ion trajectory considerably deviated from its original direction (due to redistribution of the remaining energy between parallel and perpendicular directions). The effect of elastic collisions on the distributions at the electrode depends both on the energy of the ion and its position in the sheath – an elastic collision close to the sheath-bulk interface can redistribute a large fraction of the ion energy into the perpendicular direction, but the total ion energy is low at this position and after acceleration through the sheath the perpendicular energy will be negligible compared to the parallel energy gained. Hence there will be little effect on either energy or angular distributions. The largest impact angles are obtained when the ion makes an elastic collision close to the electrode. However at this position an ion which has made no previous collisions will have a large energy (close to the sheath potential) and from Chapter 5 ions with large energies (> 10 eV) make only glancing, small-angle collisions. Substantial broadening of the IAD is therefore due either to ions which have made multiple elastic collisions in the sheath, or ions with relatively low energies (e.g. ions which have made one or more charge exchange collisions) which make an elastic collision close to the electrode surface.

Figure 6.12 (a) shows the experimental results at 10 mTorr. The IED at 2.3° indicates the ions with near normal incident angles. The high energy peak is due to ions which have crossed the sheath without making a collision, and have therefore gained the full average sheath potential. The ions at lower energy are likely to be those which have made one or more charge exchange collisions while crossing the sheath. The distributions at 11.3° and higher angles are most likely to be ions which have made one or more elastic collisions. As previously mentioned, large impact angles are most likely to occur when a low energy ion makes an elastic collision close the electrode, hence the low energy peaks which dominate the distributions at higher angles. Note that the near normal distribution has no low energy peak – the peak seen in the total energy distribution is actually due to the low energy ions at higher angles. The resemblance of the total IED to a collisionless bimodal distribution is therefore purely coincidental.

The simulation results at 2.3°, seen in Figure 6.12 (b), show *very* good agreement with the experimental results. The distributions at higher angles also show a very similar form to the experimental results, but are much smaller in magnitude particularly at the larger angles (n.b. simulation results for angles higher than 2.3° are multiplied by a factor of five in Figure 6.12 (b)). This effect has previously been discussed in terms of the total angular distributions – it is surmised that experimental measurements at non-zero impact angles have been unfairly weighted due to the larger relative areas of the annular collecting rings in the analyser. Hence the total IED for the simulation (Figure 6.6 (b)) does not have a low energy peak, because the relative magnitudes of the larger angle distributions are very much smaller than the near normal distribution. The IEDs from the Monte Carlo model by Liu *et al* also have much smaller magnitudes at non-normal angles and are scaled by a factor of 10.

The results for a pressure of 50 mTorr are shown in Figure 6.13. Experimental results at 2.3° show a strong shift toward lower energies, and prominently feature multiple peaks. Multiple peaked distributions are characteristic of charge exchange interactions in an rf sheath (Wild and Koidl (1991)). Distributions at higher angles are strongly weighted toward lower energies with large peaks between 0 and 10 eV, although 11.3° still has a small peak at about 40 eV. As for the 10 mTorr case the near normal distribution is primarily due to ions which have crossed the sheath without making a collision (although there are fewer of these at the higher pressure) or which have only made charge exchange collisions (or possibly a glancing elastic collision at high energies). The distributions at 11.3° and above are mainly due to ions which make multiple collisions.

The simulation results are very close to the experimental IEDs; particularly for 2.3°, which has a similar peaked distribution, although with the peaks shifted to slightly lower energies. The simulation results for larger angle IEDs are sharply peaked at low

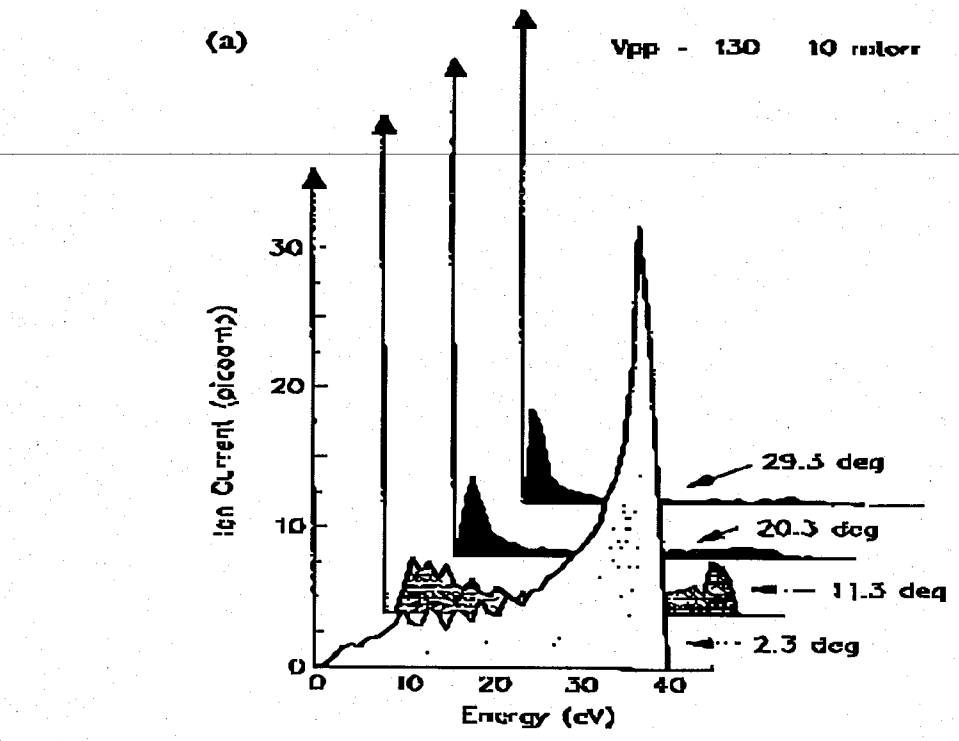

(b)

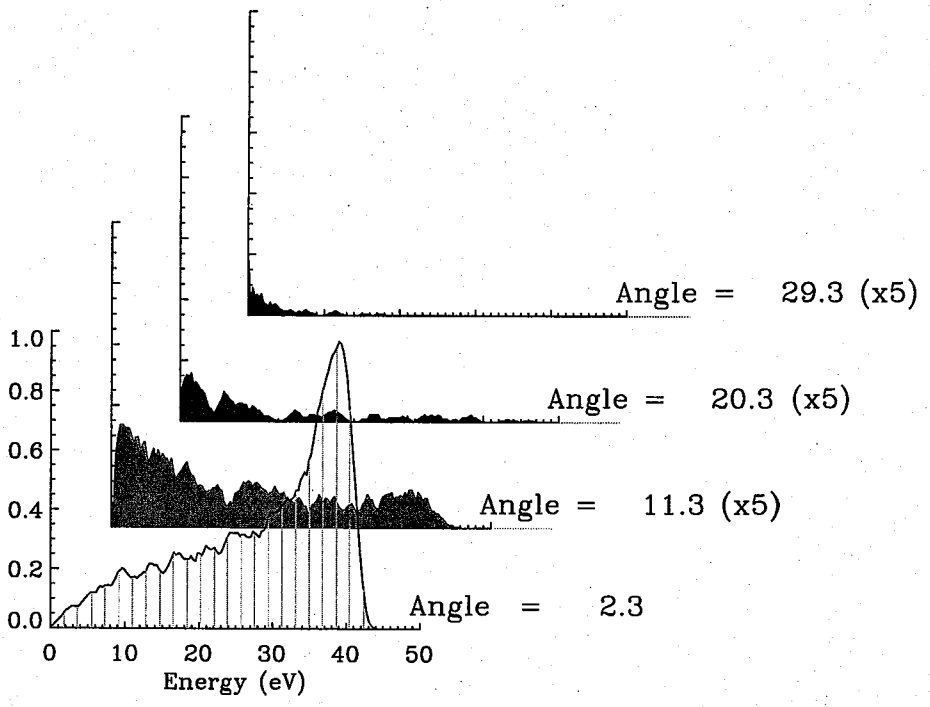

Figure 6.12 Energy distributions at specified incident angles at a pressure of $p = 10$ mTorr for **(a)** experiment (Liu *et al* (1990) **(b)** simulation (simulated results have been multiplied by 5 for 11.3°, 20.3° and 29.3°)

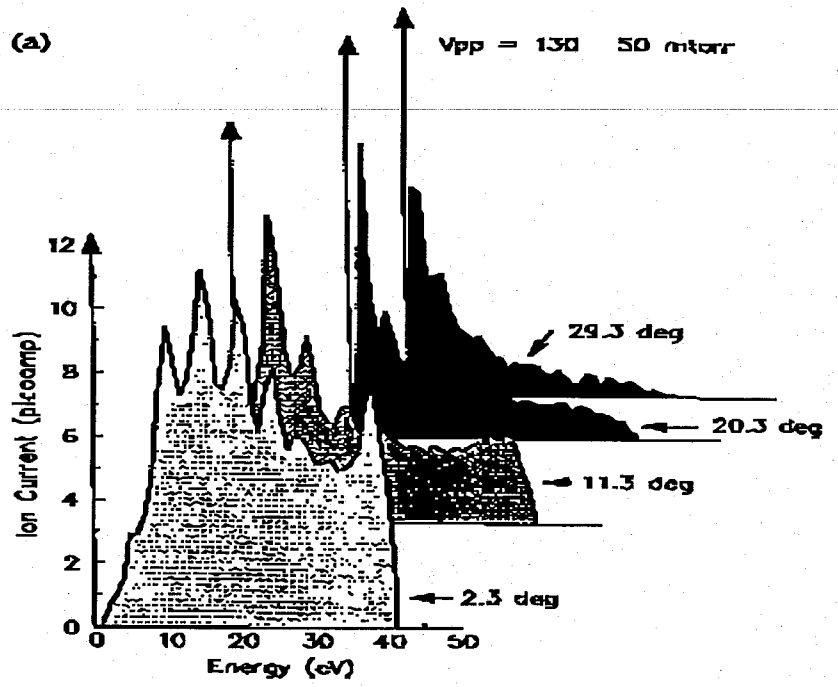

(b)

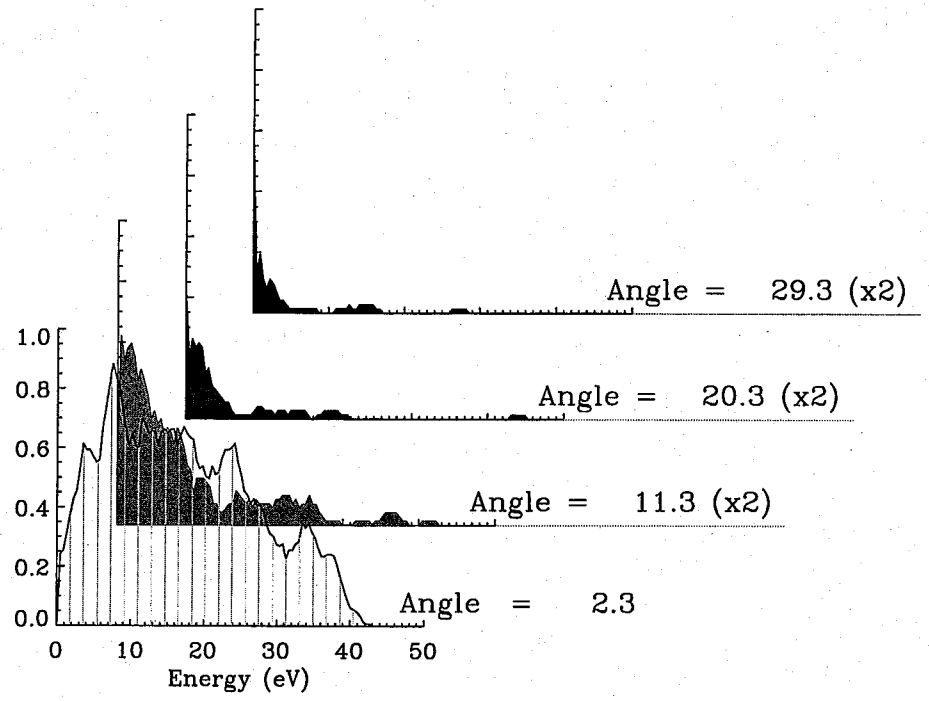

Figure 6.13 Energy distributions at specified incident angles at $p = 50$ mTorr for **(a)** experiment **(b)** simulation (simulated results have been multiplied by 2 for 11.3°, 20.3° and 29.3°).

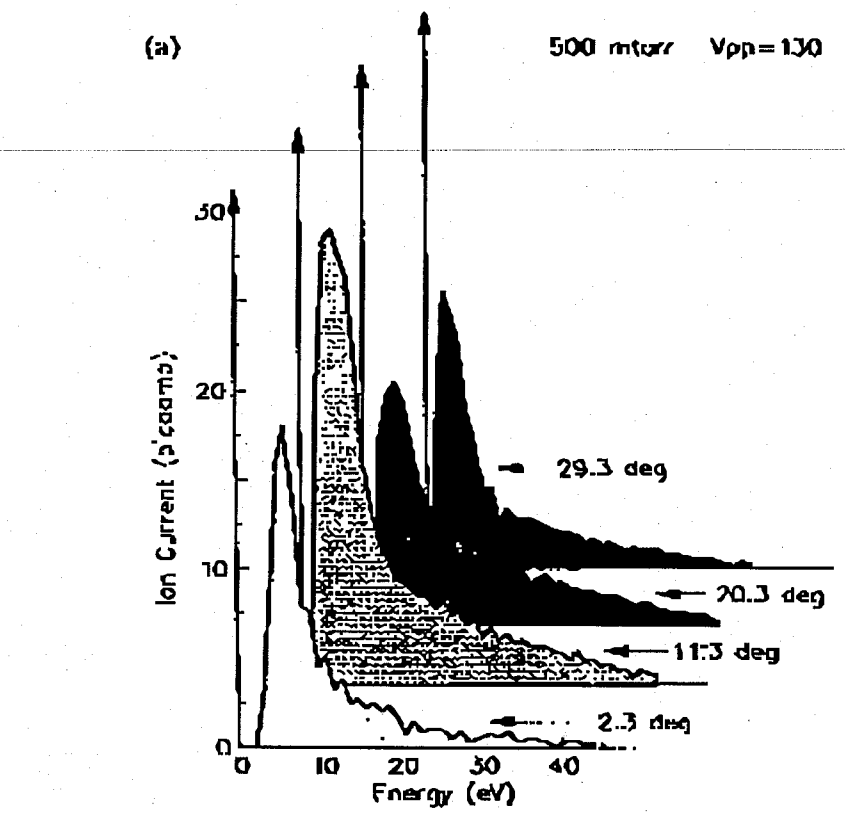

(b)

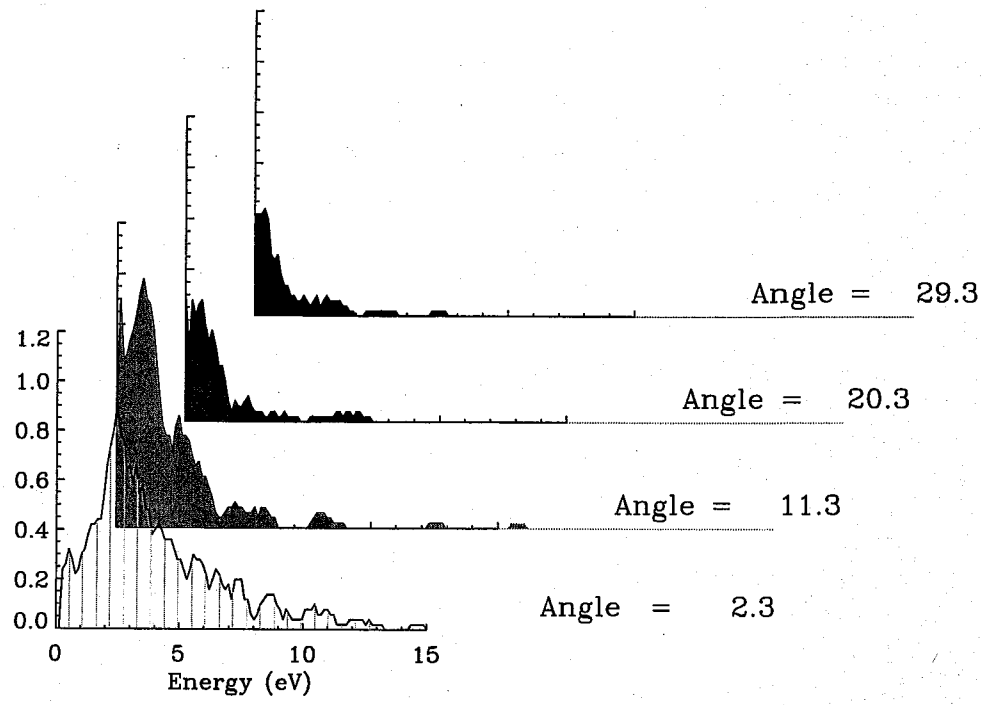

Figure 6.14 Energy distributions at specified incident angles at p = 500 mTorr for **(a)** experiment **(b)** simulation

energies, as for the experimental distributions, but also show a shift to lower energies and fewer ions are detected with the full 40 eV. As in the 10 mTorr case the relative magnitude of the non-normal distributions is much smaller than those measured experimentally and in Figure 6.12 the distributions are multiplied by a factor of two.

Finally the IEDs at a pressure of 500 mTorr are shown in Figure 6.14. The experimental results show that the distributions are very similar for all angles, all strongly peaked at low energies with roughly the same magnitude (although the distribution at 11.3° is very slightly larger than the rest). This is what Liu *et al* term a fully developed distribution, since ions undergo a large number of collisions when traversing the sheath and so the distribution is essentially isotropic.

The simulation results show a similar isotropic distribution, but shifted to lower energies. The IED at 2.3° has a low energy peak but at 3 eV rather than 7 eV and the maximum impact energy of the ions is 15 eV, rather than 45 eV. At 500 mTorr the mean free path is approximately $1/50^{th}$ of the sheath width and so it is expected that ions make multiple collisions in traversing the sheath. The simulation IEDs also show low energy structure at 1 - 2 eV which is not seen in the experimental distribution, since the energy analyser cannot measure ions with less than 2 eV. When comparing the IEDs at different angles to the total IED it can be seen that the large peak at 1 eV is mainly due to ions impacting with angles of 11.3° and higher, while the second peak at 3 eV comes from the distribution at 2.3°. The Monte Carlo IEDs are also at lower energies than measured experimentally.

Possible reasons for the shift in the simulation IEDs to lower energies relative to the experimental distributions have been discussed previously in Section 6.2.1.

6.3 Isotropic Scattering

As mentioned in the introduction, Thompson *et al* (1988) found that using either isotropic or anisotropic elastic scattering collisions made little difference to the final ion energy and angular distributions. To test this a simulation was run at a pressure of 50 mTorr in which ions collisions are modelled using the total, energy-dependent cross-sections for charge exchange and elastic scattering presented in Appendix B. When an ion makes an elastic collision an isotropic scattering angle is chosen in the centre-of-mass frame, as described in Section 2.5.1. When a charge exchange collision occurs a new velocity is chosen for the ion from a Maxwellian distribution, with a temperature of 0.025 eV.

The simulation run with isotropic scattering produced plasma conditions which were slightly different than those found using anisotropic collisions – the average density

increased by 10%, while the average ion energy decreased by 30% and the elastic collision rate by 50%. Power, electron temperature, ion current, sheath width and the charge exchange collision rate remained the same. The decrease in elastic collision rates occurs because isotropic scattering uses a "hard sphere" sphere model, in which an ion collisions occur only if the ion-neutral separation is equal to or smaller than one argon diameter. The diameter is determined from the total cross section and is therefore a function of the ion energy, with an average value of the order of 2.5 Å. The differential scattering angle model has a much larger range over which ions and neutrals can interact, and collisions can occur at impact parameters of up 3 nm. Collisions are therefore much more probable in the differential model. However, for most energies differential scattering is restricted to angles of a few degrees, whereas in the isotropic case scattering angles are much larger on average. In the isotropic simulation therefore ions have fewer, larger-angled collisions, and for anisotropic simulations they have many, small-angled collisions. Charge exchange collision rates are unaffected since both simulations use the same total cross-section. The effect of using isotropic elastic scattering on the ion distributions at the electrode is studied below.

Figure 6.16 plots the angle-dependent IEDs at 2.3°, 11.3°, 20.3° and 29.3°. The results plotted here are quite different from the anisotropic IEDs plotted in Figure 6.13(b). At 2.3° the distribution is shifted to much lower energies, with a large peak at approximately 5 eV, and the maximum energy attained by ions crossing the sheath is

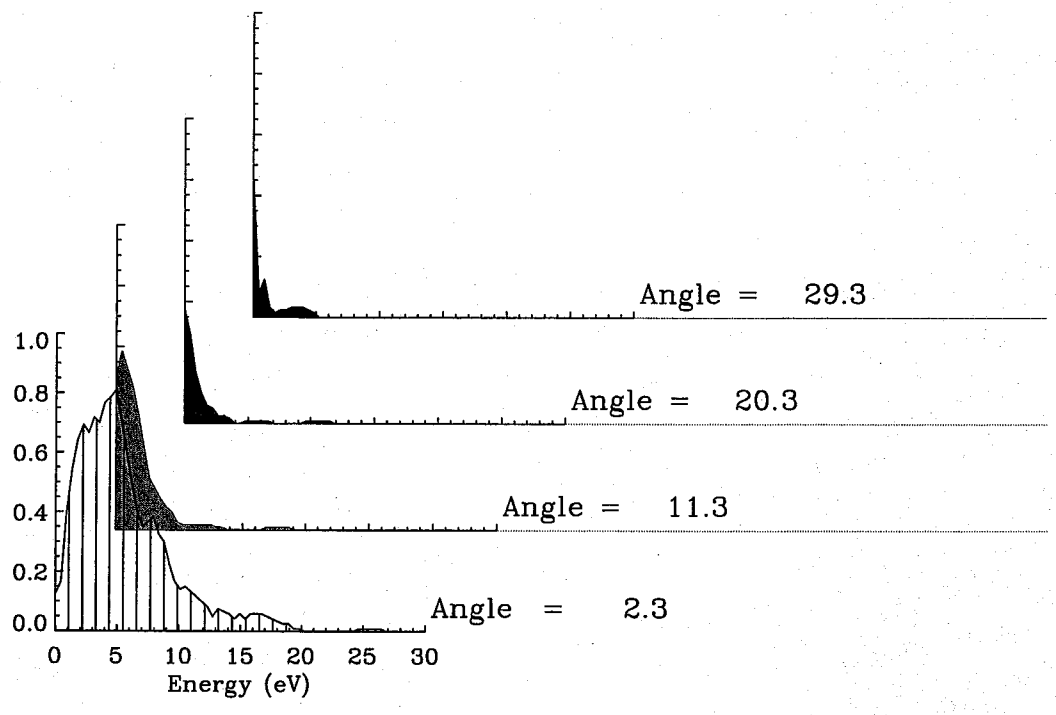

Figure 6.16 Angle dependent IEDs at p = 50 mTorr for isotropically scattered ions.

reduced to 20 eV. The distributions at higher angles are much larger (note they are not magnified as is the case for the anisotropic distributions) and also show a shift to lower energies. The average impact energy of ions at the electrode for the isotropic case is 10 eV, which is 10 % lower than for the anisotropic case.

The charge exchange collision rate is unchanged from the anisotropic case, so the differences between the two cases must be entirely due to elastic collisions. The increase in magnitude of large angle scattering distributions comes about because in the isotropic case scattering angles are on average much larger than for anisotropic scattering. The shift to lower energies occurs because at large scattering angles more energy is transferred to the neutrals. Hence, although the elastic collision rate has reduced, more energy is lost per interaction leading to a net greater energy loss from the ions. It therefore seems apparent from these results that the form of the elastic collision cross section is important in determining distributions at the electrode.

6.5 Conclusion

In this chapter results from PIC simulations of a planar argon plasma, which includes a differential cross-section model for ion-neutral collisions, have been compared to experimentally measured ion distributions at the electrodes. In particular total ion energy and angular distributions and angle-dependent energy distributions have been examined. For a range of pressures the simulation distributions have a similar form to the experimental measurements, and at certain conditions (near normal incident angles and low pressures) both match exactly. There are two main differences found between simulation and experiment, one related to angular and the other to energy measurements. Experimental measurements made at non-normal incident angles were found to be much larger than simulation results – this has been attributed to the ion analyser, and corrected values are presented in Section 6.2.2. Simulation results also show IEDs which are shifted to lower energies at high pressures than the experimental results. It has been hypothesised that this could be due to a reduction in the number of plasma species and their interactions in the simulation, and also a simplification of the reactor/analyser geometry.

The form of the elastic scattering was also found to be important, contradicting the findings of Thompson *et al* (1988). Isotropic elastic scattering collisions were found to shift the ion energy distribution to lower energies, and substantially increase the magnitude of the IAD at large angles, in comparison to results from anisotropic scattering. These results therefore underestimate the average ion bombardment energy at the electrode and overestimate the average impact angle.

Appendix A
Fitting to Experimental Cross-sections

Binary collisions between charged particles and neutrals are modelled in the simulation using Monte Carlo techniques. Most of the simulations assume isotropic scattering of electrons and ions and a description of this collision process is given in Chapter 2. In order to determine the collision probability it is necessary to know each cross-section as a function of energy – this Appendix details the ion and electron cross-section for atomic hydrogen and argon. All simulation cross-sections are determined by fitting to experimental data.

Electron Cross-sections:

Ionisation and excitation cross-sections are both fitted by an equation with the form

$$Q(x) = \frac{Q_o}{x^b \varepsilon_{th}^2}\left(\frac{ax-a}{ax+1}\right)^c, \qquad \text{A.1}$$

where $x = \varepsilon/\varepsilon_{th}$, ε is the ion energy (in eV), ε_{th} is the threshold energy for the collision to occur and Q_o, a, b and c are fitting factors dependent on the neutral species.

Elastic cross-sections are fitted individually, depending on the form of the cross-section.

Ion Cross-sections

Both charge exchange and elastic scattering cross-sections can be fitted using

$$Q(\varepsilon) = (a - b\ln\varepsilon)^2 \times 10^{-20} \qquad \text{(A.2)}$$

where ε is the ion energy in eV, and a and b are fitting parameters depending on the gas type.

Pseudo cross-sections for both electrons and ions are fitted using:

$$Q_{pseudo} = \frac{Q_o}{v} \qquad \text{(A.3)}$$

where Q_o is a fitting parameter and v is the particle velocity.

A.1 e⁻-H cross-sections

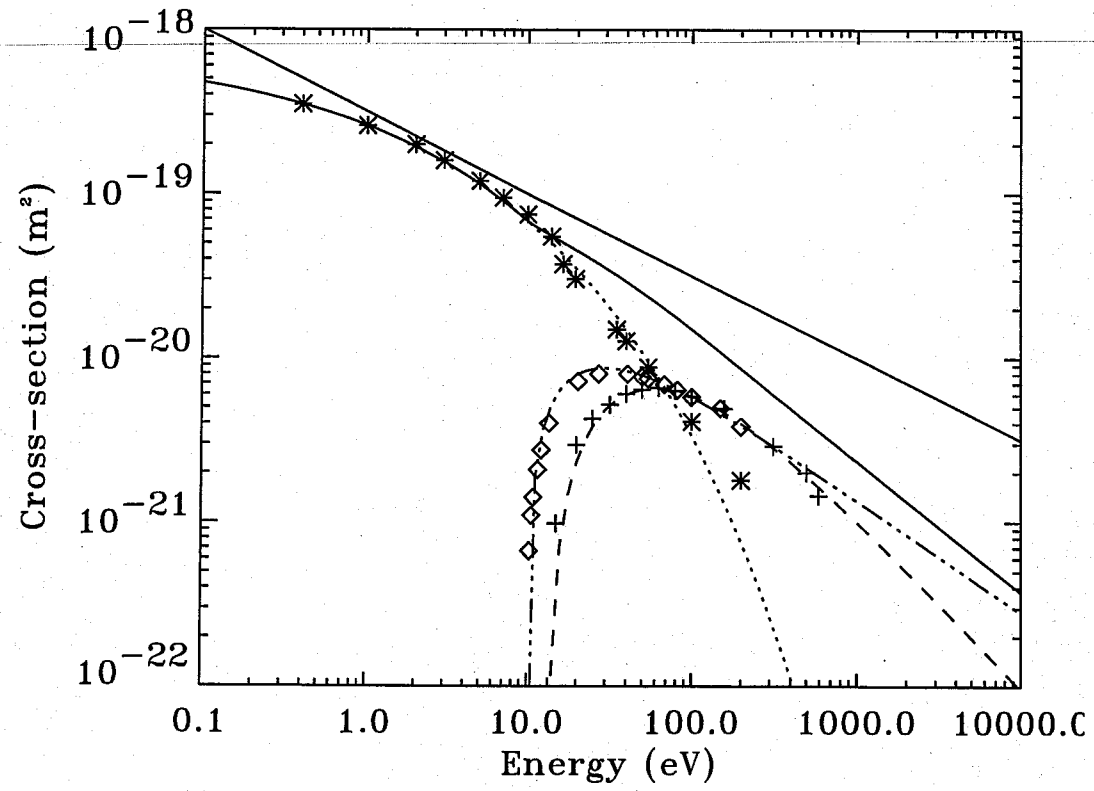

Figure A.1 e⁻-H cross-sections as a function of energy, including elastic scattering (dotted line), ionisation (dashed line), excitation (dash-dot line), total cross-section (solid line) and pseudo fit (thick line). Experimental results are shown as symbols.

Ionisation:

ε_{th} = 13.5 eV
Q_o = 1.81x10^{-17} m^2
a = 0.333, b = 1.05 and c = 1.5

Experimental data is from Kieffer and Dunn (1966)

Excitation:

ε_{th} = 10.2 eV,
Q_o = 3.50x10^{-18} m^2
a = 1.7, b = 0.70 and c = 1.0

Experimental data is from McDowell *et al* (1975)

Elastic Scattering

The elastic cross-section is fitted using an exponential with the form

$$Q_{elas} = 7.68 \times 10^{-19} e^{-1.0834 \varepsilon^{0.35}}$$

where ε is the electron energy in eV.

Experimental data for: 0.4-14 eV is from Brackman *et al* (1958)
16.48 - 200 eV is from Dimitry *et al* (1991)

Pseudo cross-section fit:

$Q_{pseudo} = 1.875 \text{x} 10^{-13}/v$ m^2

A.2 e⁻-Ar cross-sections

The elastic cross-section for electron-argon collisions is a little more difficult to fit due to the presence of the Ramsauer minimum at 0.345 eV. To take this into account the elastic cross-section has been separated into three energy regions and each region is fitted with a separate power law. To reduce the number of null collisions that the electrons make at low energies the pseudo cross-section is also divided into two separate fitting regions.

Ionisation:

$\varepsilon_{th} = 15.759$ eV
$Q_o = 6.5 \text{x} 10^{-17}$ m^2
$a = 0.5$, $b = 0.87$ and $c = 1.4$

Experimental data is from Krishnakumar and Srivastura (1988)

Excitation:

$\varepsilon_{th} = 11.6$ eV
$Q_o = 1.1 \text{x} 10^{-17}$ m^2
$a = 0.18$, $b = 0.85$ and $c = 1.0$

Experimental data is from de Heer *et al* (1979)

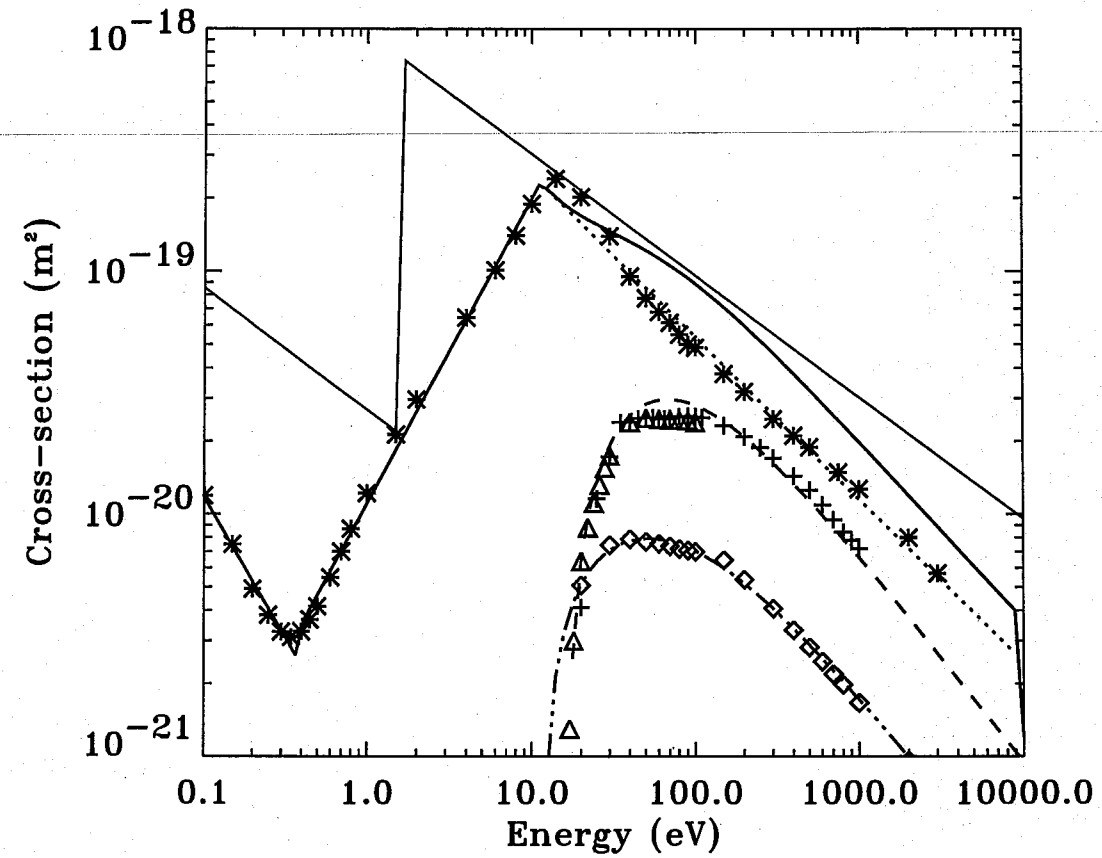

Figure A.2 e^--Ar cross-sections as a function of energy, including elastic scattering (dotted line), ionisation (dashed line), excitation (dash-dot line), total cross-section (solid line) and pseudo fit (thick line). Experimental results are shown as symbols.

Elastic Scattering:

$0 < \varepsilon < 0.34$ eV	$Q_{elas} = 8.324\text{x}10^{-22}\varepsilon^{-1.15}$ m^2
$0.34 < \varepsilon < 12.0$ eV	$Q_{elas} = 1.105\text{x}10^{-20}\varepsilon^{1.26}$ m^2
$\varepsilon > 12.0$ eV	$Q_{elas} = 1.17\text{x}10^{-18}\varepsilon^{-0.07}$ m^2
Experimental data for:	0.0 - 20.0 eV is from Ferch *et al* (1985)
	20.0 - 3000.0 eV is from de Heer *et al* (1979)

Pseudo cross-section fit:

$0 < \varepsilon < 1.9$ eV	$Q_{pseudo} = 1.6\text{x}10^{-14}/v$ m^2
$\varepsilon > 1.9$ eV	$Q_{pseudo} = 5.7\text{x}10^{-13}/v$ m^2

A.3 H+-H cross-sections

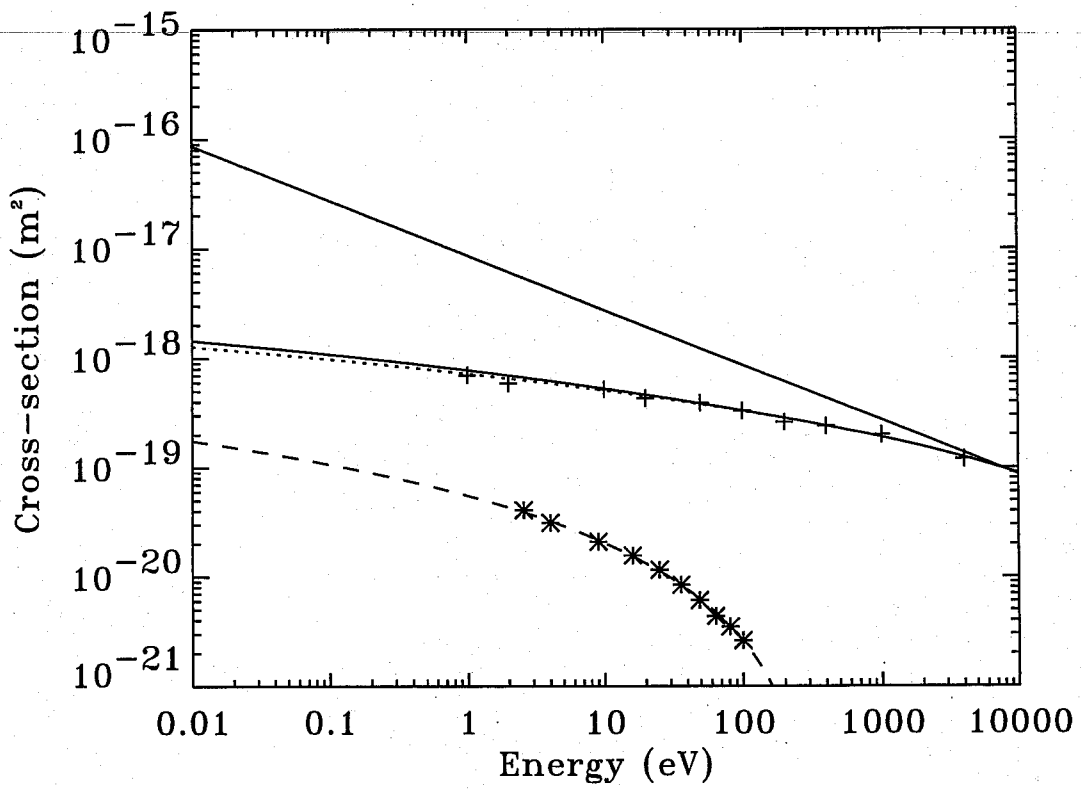

Figure A.3 H^+-H cross-sections as a function of energy, including elastic scattering (dashed line), charge exchange (dotted line), the total cross-section (solid line) and pseudo fit (thick line). Experimental results are shown as symbols.

Elastic scattering:

$a = 2.35$ $b = 0.40$

Experimental data is from McDaniel (1964, pg 253)

Charge exchange:

$a = 8.5$ $b = 0.6$

Experimental data is from McDaniel (1964, pg 253)

Pseudo cross-section fit:

$$Q_{pseudo} = 2.0\text{x}10^{-14}/v \text{ m}^2$$

A.4 Ar+-Ar cross-sections

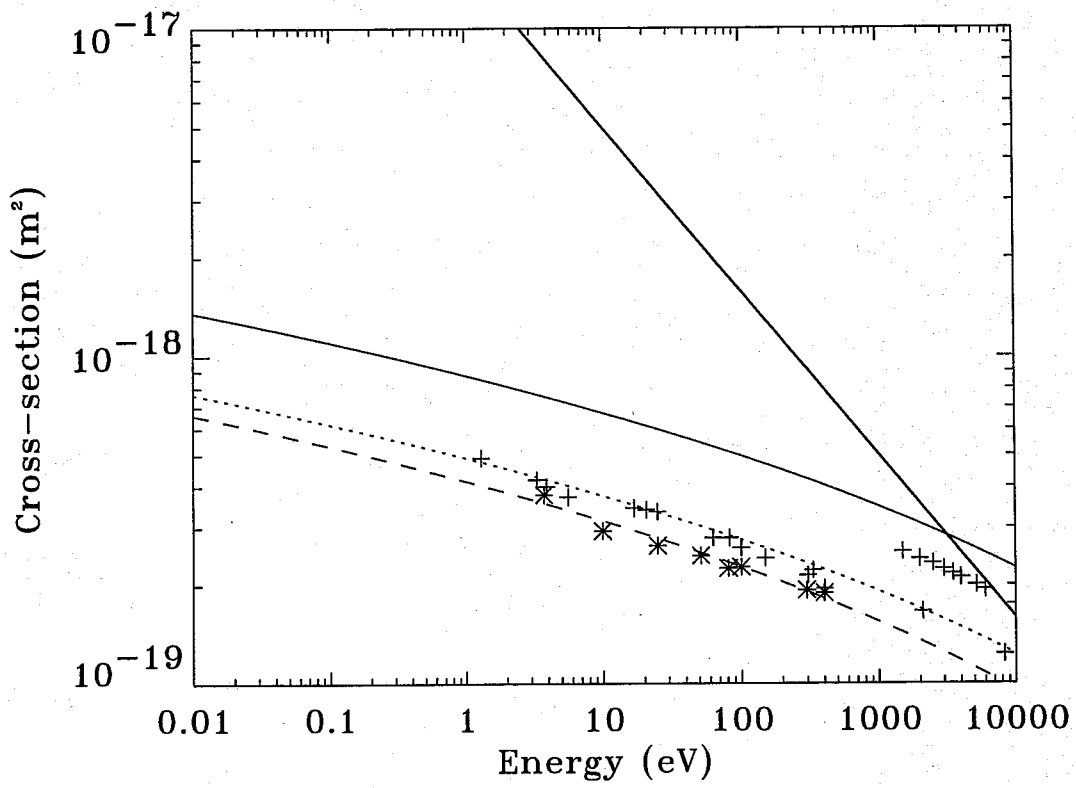

Figure A.4 Ar^+-Ar cross-sections as a function of energy, including elastic scattering (dashed line), charge exchange (dotted line), the total cross-section (solid line) and pseudo fit (thick line). Experimental results are shown as symbols (triangles are charge exchange data)

Elastic scattering:

$a = 6.45$ $b = 0.365$

Experimental data is from McDaniel (1964)

Charge exchange:

$a = 8.5$ $b = 0.6$

Experimental data for: 4 - 400 eV is from McDaniel (1964)
0 - 8 keV is from Rapp and Francis (1962)
1.5 - 200 keV is from Hegerberg *et al* (1978)

Pseudo cross-section fit:

$$Q_{pseudo} = 3.5\text{x}10^{-14}/v \text{ m}^2$$

Note that the experimental charge exchange cross-sections shown in Figure A.4 are quite different for high and low energies. Although the data at high energy (Hegerberg *et al* (1978)) is more recent, the fitting was made to data from McDaniel (1964) and Rapp and Francis (1962), since these are in the energy range of interest. However it is interesting to note that either the cross-sections alter drastically at high energies, or else there is a large discrepancy between experimental measurements. Figure A.4 also shows that the pseudo cross-section used here is only valid for ion energies up to 2000 eV. This value was chosen as a cutoff in order to reduce computational time, which increases with increasing magnitude of Q_{pseudo} due to the reduced mean free time between collisions.

Appendix B
Ionisation cross-section of hydrogen as a function of kTe

The electron-hydrogen collision frequency for a given interaction is $N\langle Qv\rangle$, where N is the neutral gas density, Q the cross-section for that interaction and < > denotes the average over the electron velocity distribution $f(v)$. The average cross-section is then given by:

$$\overline{Q} = \frac{\langle Qv\rangle}{\langle v\rangle} \tag{B.1}$$

Asuming that the electrons have a Maxwellian distribution, then $f(v) \propto v^2 e^{-\frac{mv^2}{2kTe}}$. Averaging over the distribution $\langle Qv\rangle$ is given by

$$\begin{aligned}\langle Q.v\rangle &= \frac{\int_0^\infty Qvf(v)dv}{\int_0^\infty f(v)dv} \\ &= \left(\frac{2e}{m_e}\right)^{1/2} \frac{\int_0^\infty Q(\varepsilon)e^{-\varepsilon/kT_e}d\varepsilon}{\int_0^\infty \varepsilon^{-1/2}e^{-\varepsilon/kT_e}d\varepsilon}.\end{aligned} \tag{B.2}$$

where m_e, e and ε are the mass, charge and energy (in eV) of the electron respectively. It should be noted that the average ionisation rate is very sensitive to the electron temperature, and a slight non-Maxwellian increase in the tail of the electron distribution can have a large effect on the calculated value of $\langle Qv\rangle$.

Combining (B.1) and (B.2) and substituting in the average velocity of a Maxwellian distribution, $\langle v\rangle = \sqrt{\frac{8kT_e}{\pi m_e}}$ gives

$$\overline{Q}(kTe) = \left(\frac{e\pi}{4kT_e}\right)^{1/2} \frac{\int_0^\infty Q(\varepsilon)e^{-\varepsilon/kT_e}d\varepsilon}{\int_0^\infty \varepsilon^{-1/2}e^{-\varepsilon/kT_e}d\varepsilon}. \tag{B.3}$$

then $Q_{ion}(kT_e)$ can be integrated numerically, using $Q_{ion}(\varepsilon)$ determined from equation (A.1), with the appropriate constants. This is plotted in Figure B.1.

Fitting (B.3) with an exponential curve, gives an equation of the form

$$Q_{ion}(kT_e) = Q_o e^{-\varepsilon_{ion}/kT_e},$$

where Q_o = 8.2x10^{-21} m^2. This is also plotted as a dotted line in Figure B.1, and shows good agreement with the numerical derivation to electron temperatures of around 20 eV, which is adequate for most applications to the simulations, which have an average temperature of 3.5 eV.

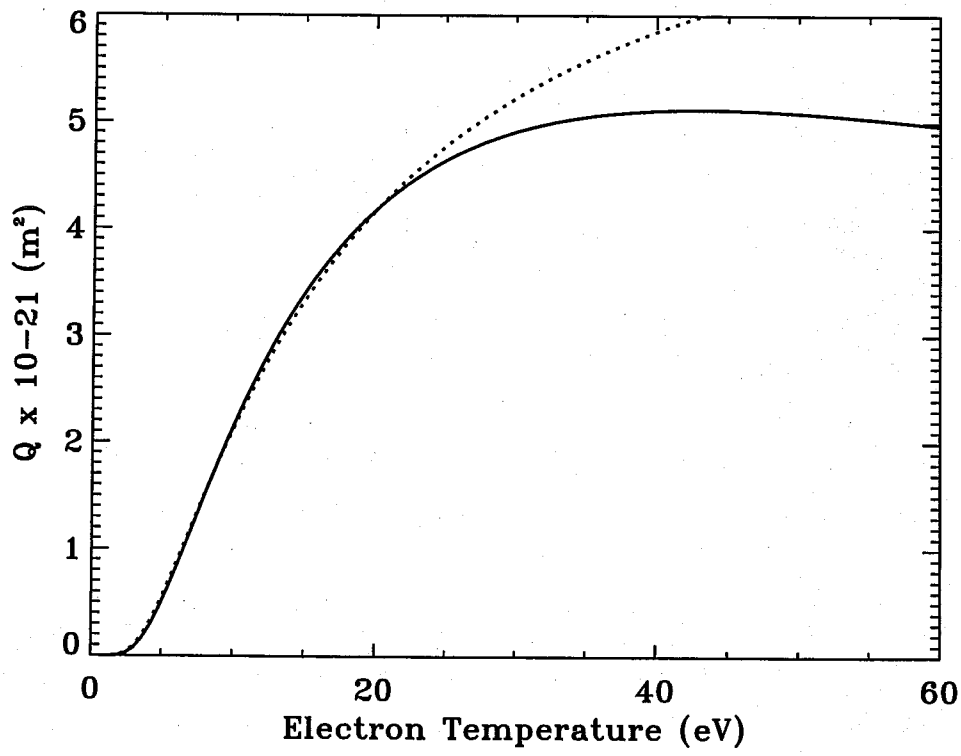

Figure B.1 The average ionisation cross-section Q_{ion} determined as a function of the electron temperature. The solid line shows the numerical solution of Q_{ion} using (B.3), and the dotted line the exponential fit to this.